Failure mechanism of nano-structural interfacial layer in Mg matrix composites reinforced with Cf

W.G. Wang [a,b], J.F. Zhang [b], Y.N. Zan [b], Z.Y. Liu [b], D. Wang [b], B.L. Xiao [b,*], D.R. Ni [b], Z.Y. Ma [b,*]

[a] School of Mechanical Engineering, Liaoning Shihua University, Xiduan No.1, Dandong Road, Fushun 113001, China
[b] Shi-changxu Innovation Center for Advanced Materials, Institute of Metal Research, Chinese Academy of Sciences, 72 Wenhua Road, Shenyang 110016, China

ARTICLE INFO

ABSTRACT

The surface of continuous carbon fibers (Cf) was modified with γ-Al_2O_3, anatase-TiO_2 and yttria stabilized zirconia (YSZ) coatings in sol-gel route, and denoted by Al_2O_3@Cf, TiO_2@Cf and YSZ@Cf, respectively. Following, Cf/Mg composites were prepared using vacuum pressureless infiltration processing. Except for coatings, the others preparation process parameters were same. Independent of the volume fraction of Cf, the **strengthening ratio** (the ratio of measured tensile strength to theoretically predicted value) of Al_2O_3@Cf/Mg, TiO_2@Cf/Mg and YSZ@Cf/Mg is about 45%, 80% and 90%, respectively. In view of high resolution transmission electron microscope observation, the evolutions of interfacial micro-cracks and interfacial failure mechanisms were analyzed. In YSZ@Cf/Mg, the interfacial micro-crack was more likely to initiate at the soft grain boundaries (GBs) of interfacial layer (IL), and then propagate along GBs within IL, showing jagged-like morphology. The jagged-like micro-cracks would consume more destructive energy, resulting into the excellent performance of YSZ@Cf/Mg.

1. Introduction

Continuous fibers (Cf) reinforced Mg matrix composites (Cf/Mg) have some superior properties [1–9], such as low weight [7–9], high strength [7–11], high elastic modulus [4,7], and low coefficient of thermal expansion (CTE) [12–14] etc., but there are still some problems waiting to be solved. Specially, the interface control has always been the important factor to restrict the preparations and applications of Cf reinforced metal matrix composites [8–11,15–17].

It was documented that Cf has a weak interaction with all kinds of metal matrices [1]. Moreover, there are many huge differences in the intrinsic properties between Cf and metal matrix. On one hand, the wettability between Cf and matrix must be improved to control the interface. On the other hand, the problems of mechanical (load transfer and interfacial thermal residual stress etc.), chemical (interfacial reaction) and physical (thermal conductivity etc.) compatibilities should also be solved. In these respects, a large number of studies have been carried out, in which the modification of the Cf surface using coatings was the most conventional and effective method [10,18–26].

Up to now, many coating processes have been developed, such as sol–gel [8,9,22], chemical vapor deposition (CVD) [10,18–20], molten salt process [23,24], electroplating or electroless plating [25–27], etc. In the subsequent preparation process of composites, these coatings would react with the metal matrix and Cf to form interfacial layer (IL), and most of these IL were nanostructure [8–10,23,26–30].

So far, some researchers believed that the weak interface was beneficial to the tensile properties of Cf reinforced metal matrix composites [11,16,31–33], because crack propagation could be stopped [11,16] and deflected [16] at the soft interface. But at the same time, other scholars believed that a weak interfacial bonding would not lead to favorable mechanical performance [1,34,35]. Recently, it was documented [36] that the interfacial bonding strength between Cf and matrix should be neither too strong nor too weak. The main reason for these disagreements should be attributed to the insufficient observations and analyses on the nanostructure of the interface and/or IL, due to the limitation of analytical test methods which could be able accurately to measure the interphase characteristics on nanoscale level [20].

In our previous studies [8,9], taking account of the advantages of sol–gel method such as lower cost, controllability of coating thickness and nano-grains size, the surface of Cf was modified with γ-Al_2O_3, anatase-TiO_2 and yttria stabilized zirconia (YSZ) coatings in sol–gel route, respectively. Following, the Cf/Mg composites were fabricated

with vacuum pressureless infiltration processing. Although it was clarified that the IL (about 20 nm thick) were formed mainly by MgO nano-grains and a small quantities of TiC, ZrC and ZrO$_2$ nano-grains, unfortunately, there is still a lack of direct observational report about the initiation and propagation of interfacial micro-cracks at the nanoscale. This is not only because of the small scale, but also because of the disordered crystal orientation among the nano-grains of IL, metal matrix and C$_f$.

As a continuation of our previous work [8,9], to clarify the relationships among interfacial nanostructures, interfacial failure behaviors and the mechanical properties of C$_f$/Mg, the microstructures of interfacial micro-cracks were observed with high resolution transmission electron microscope (HRTEM), and then the initiation and propagation mechanism of interfacial micro-crack in C$_f$/Mg composites were analyzed in this study.

2. Material and methods

2.1. Preparation of C$_f$ preforms

Unidirectionally aligned PAN based C$_f$ with density of 1.8 g/cm^3 (diameter of 7 µm, Dalian Xingke Carbon Fiber Company Ltd., China) was used in this study. The preform of 60 × 25 × 5 mm containing about 35 vol% and 45 vol% C$_f$ were prepared by a filament winding technique, respectively. In order to remove the sizing agent on the surfaces of C$_f$, the preforms were heated at 450 °C for 30 min in a vacuum furnace. After removing the sizing agent, the tensile strength of C$_f$ was tested to be 2.6 GPa, according to the ASTM D3379-75 standard [37].

2.2. Preparation of sol–gel coating

In order to contradistinguish and study the interfacial failure behaviors in C$_f$/Mg, the surface of C$_f$ was modified with γ-Al$_2$O$_3$, anatase-TiO$_2$ and YSZ coating using sol–gel method, respectively. The preparation methods of these coatings were described in previous studies [8,9].

2.3. Fabrication of C$_f$/Mg composite

The pure Mg matrix composites reinforced with 35 vol% and 45 vol% C$_f$ were fabricated using pressureless infiltration process in vacuum [8,9], respectively. Since the thickness of the coatings (about 20 nm) on the surface of C$_f$ was very small, as compared with the diameter of C$_f$ (7 µm), indicating that the volume of coatings could be neglected. As the first step, commercial Mg ingots and C$_f$ preforms were sealed in a steel die. Then they were heated in a vacuum furnace to 750 °C, and the temperature was maintained for about 30 min to achieve the liquid metal infiltration. After the infiltration, the C$_f$/Mg was cooled down in the vacuum furnace. The Mg matrix composites reinforced by C$_f$ coated with γ-Al$_2$O$_3$, anatase-TiO$_2$ and YSZ coating were denoted by Al$_2$O$_3$@C$_f$/Mg, TiO$_2$@C$_f$/Mg and YSZ@C$_f$/Mg, respectively.

2.4. Characterization

The gauge length, width and thickness of tensile specimens of C$_f$/Mg was 10.0 mm, 2.0 mm and a 1.5 mm, respectively. And the tensile direction of samples was parallel to the longitudinal direction of C$_f$. Tensile tests were conducted at room temperature and an initial strain rate of 3.3 × 10^{-4} s^{-1} on Zwick/RoellZ050 tester. Then, the tensile fractograph of C$_f$/Mg was examined using scanning electron microscopy (SEM, Nova NanoSEM 430). The density of C$_f$/Mg composite was measured by buoyancy method.

In order to clarify the evolution of interfacial micro-cracks, the observations with transmission electron microscopy (TEM, Tecnai G2 20) were carried out. As well known, in-situ tensile observation is an important route to study the interfacial failure behaviors at nano-scale. Unfortunately, the TEM foil is so thin that the onion-skin structure [38]

of C$_f$ would be destroyed and the C$_f$ foil could not bear loading due to the poor shearing strength of $(0\,0\,1)_{graphite}$ basal plane. Therefore, in this study, the C$_f$/Mg was pre-stretched (50% and 80% of its tensile strength). And then, the slices were cut from the pre-stretched C$_f$/Mg perpendicular to the longitudinal direction of C$_f$, and then the thin foils for TEM observation were prepared by the ion milling technique.

3. Results

3.1. The micrographs and tensile properties

Fig. 1 show the SEM micrographs of Mg matrix composite reinforced with Al$_2$O$_3$@C$_f$, TiO$_2$@C$_f$ and YSZ@C$_f$. After infiltration, the Mg matrix could infiltrate into the space among C$_f$, and no obvious voids or other defects could be found. The average fiber spacing were 2.33 µm and 2.0 µm in 35 vol% C$_f$/Mg and 45 vol% C$_f$/Mg, respectively. Additionally, the density of 35 vol% and 45 vol% C$_f$ reinforced Mg matrix composites were 1.76 and 1.77 g/cm^3, respectively. The measured density was very close to the theoretical values, indicating that the C$_f$/Mg composites were dense.

Combined with the results of previous researches [8,9] and this study, the tensile strengths of C$_f$/Mg are listed in Table 1. With the same volume fraction of C$_f$, the Al$_2$O$_3$@C$_f$/Mg and YSZ@C$_f$/Mg showed the lowest and highest tensile strength, respectively. At the same time, the YSZ@C$_f$/Mg with the C$_f$ volume fraction of 35 vol% and 45 vol% exhibited the tensile strength of 850 MPa and 1080 MPa (Table 1), respectively, which reach 90% of the theoretical prediction by means of the rule of mixture. In contrast, the Al$_2$O$_3$@C$_f$/Mg showed the lowest strength, which was 410 MPa and 550 MPa (Table 1), respectively.

In order to better evaluate the strengthening efficiency of C$_f$ and provide data support for the optimization design of C$_f$/Mg, "***strengthening ratio***" (the ratio of measured tensile strength to the theoretically predicted value) was introduced in this study. The theoretically predicted value and strengthening ratio (γ) could be obtained as follows:

$$\sigma_{theoretical\ value} = \sigma_f \cdot V_f + \sigma_m \cdot (1 - V_f) \tag{1}$$

$$\gamma = \frac{\sigma_{composite}}{\sigma_{theoretical\ value}} \cdot 100\% \tag{2}$$

Where the σ_f and V_f are the tensile strength and volume fraction of C$_f$, respectively; σ_m and $\sigma_{composite}$ are the tensile strength of matrix and composite, respectively.

As shown in Table 1, whether the volume fraction of C$_f$ are 35% or 45%, the ***strengthening ratio*** of Al$_2$O$_3$@C$_f$/Mg, TiO$_2$@C$_f$/Mg and YSZ@C$_f$/Mg are about 45%, 80% and 90%, respectively. It is very attractive that the strengthening ratio was unrelated to the volume fraction of C$_f$ but dominated by the surface coatings on the C$_f$, because the preparation process of C$_f$/Mg composite are same (including the thickness of coating), except for the chemical composition of coating. Furthermore, the strengthening ratio should be determined by the nanostructures of IL, because the coating would react with the Mg matrix to form IL during the preparation of C$_f$/Mg [8].

3.2. The fracture morphology

Since the volume fraction of C$_f$ had little effect on the strengthening ratio of C$_f$/Mg, 45 vol% C$_f$ reinforced Mg matrix composites were selected as the representatives to study the failure behaviors. Fig. 2(a) shows the tensile fractograph of Al$_2$O$_3$@C$_f$/Mg under lower magnification. According to the SEM observation, some C$_f$ bundles were pulled out from the matrix, and these C$_f$ bundles were composed of about 10 fibers (Fig. 2(b)). Moreover, on the side surface of C$_f$, some annular steps marked with *A* and *B* could be observed, as shown in Fig. 2(b). According to the EDS analysis, the main element at point A was carbon, while the elements at point B included carbon (89.89 atomic%), magnesium (5.93 atomic%) and oxygen (4.18 atomic%). Considering the
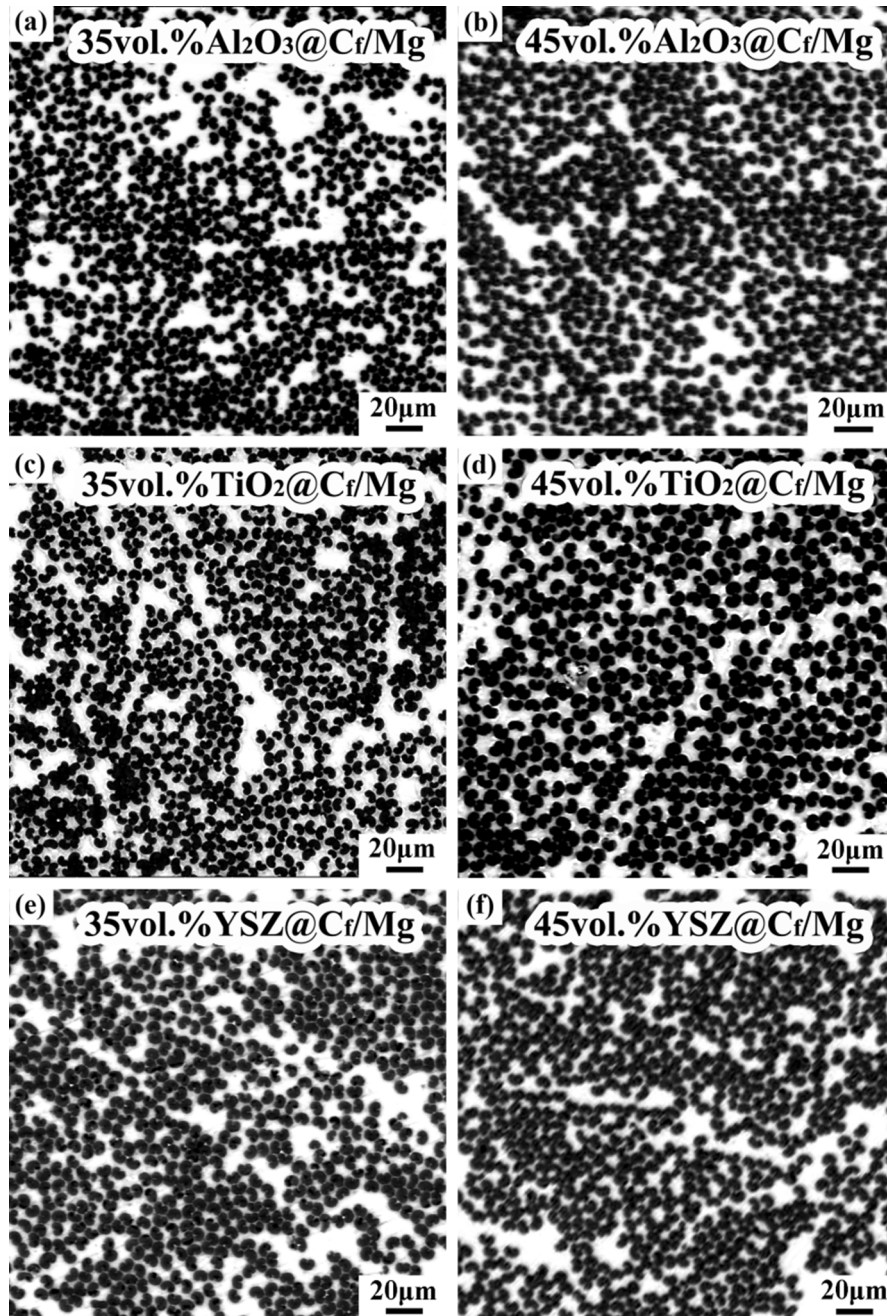
Fig 1. SEM micrographs showing microstructures of 35 vol% and 45 vol% C_f reinforced Mg matrix composites: (a) and (b) Al_2O_3 coatings, (c) and (d) TiO_2 coating, (e) and (f) YSZ coating.

oxidation of Mg matrix, it can be thought that the actual oxygen concentration was not as high as 4.18 atomic%. According to the previous studies [8], there was an IL between C_f and Mg matrix in $Al_2O_3@C_f/Mg$, and the IL was mainly composed of MgO nano-grains due to the interfacial reaction. This indicates that the Mg matrix and IL were completely pulled out from the surface of C_f at point A.

Fig. 2(c) and (d) show the tensile fractograph of 45 vol.%$TiO_2@C_f/$ Mg under lower and higher magnifications, respectively, while Fig. 2(e) and (f) are the tensile fractographs of 45vol.%$YSZ@C_f/Mg$. For $TiO_2@C_f/Mg$ and $YSZ@C_f/Mg$, the C_f bundles pulled out from matrix were composed of about dozens of C_f. Compared with that in $Al_2O_3@C_f/$ Mg, the number of pulled-out C_f per bundle increased significantly in $TiO_2@C_f/Mg$ and $YSZ@C_f/Mg$, as shown in Fig. 2(c) and (e). Particularly, no annular step could be found on the tensile fractographs of $TiO_2@C_f/Mg$ and $YSZ@C_f/Mg$. This indicates that the interfacial failure

mechanism in $Al_2O_3@C_f/Mg$ is different with that in $TiO_2@C_f/Mg$ or $YSZ@C_f/Mg$.

3.3. The microstructures and evolution of interfacial micro-crack

According to the previous results of HRTEM observations [8,9], the microstructure of IL in $Al_2O_3@C_f/Mg$ [8] was different from those in $TiO_2@C_f/Mg$ [8] and $YSZ@C_f/Mg$ [9], though the thickness of IL were same. On one hand, the grain size of the IL in $Al_2O_3@C_f/Mg$ was relatively large (10–20 nm). On the other hand, there was no carbide formation in $Al_2O_3@C_f/Mg$. On the contrast, the grain size of the IL in $TiO_2@C_f/Mg$ and $YSZ@C_f/Mg$ were only 3–5 nm, and there were TiC and ZrC nano-grains in the IL of $TiO_2@C_f/Mg$ and $YSZ@C_f/Mg$, respectively. Therefore, in this study, the $Al_2O_3@C_f/Mg$ and $YSZ@C_f/$ Mg with the lowest and highest ***strengthening ratio*** were selected as

Table 1
The measured and theoretical values of tensile strength of Al$_2$O$_3$@C$_f$/Mg, TiO$_2$@ C$_f$/Mg and YSZ@ C$_f$/Mg.

CfMMCs	Measured value (MPa)	Theoretical value (MPa)	Strengthening ratio
35 vol% Al$_2$O$_3$@C$_f$/Mg	410	940	43.6%
45 vol% Al$_2$O$_3$@C$_f$/Mg	550 [8]	1200	45.8% [8]
35 vol% TiO$_2$@C$_f$/Mg	760	940	80.9%
45 vol% TiO$_2$@C$_f$/Mg	980 [8]	1200	81.7% [8]
35 vol% YSZ@C$_f$/Mg	850	940	90.4%
45 vol% YSZ@C$_f$/Mg	1080 [9]	1200	90.0% [9]

typical representatives, and the evolution mechanism of interfacial micro-cracks was observed and analyzed from the nanoscale.

At first, 45vol.%Al$_2$O$_3$@C$_f$/Mg was pre-stretched to 440 MPa (80% of its tensile strength of 550 MPa), and 45vol.%YSZ@C$_f$/Mg was pre-stretched to 540 MPa (50% of its tensile strength of 1080 MPa). Then, the pre-stretched samples were observed with TEM, as shown in Figs. 3 and 4. While some interfacial micro-cracks formed in Al$_2$O$_3$@C$_f$/Mg (Fig. 3 (a)), no obvious interfacial damage could be found in YSZ@C$_f$/Mg (Fig. 4 (a)), even if the latter's pre-tension stress was greater. Moreover, a high density of dislocations in the matrices nearby the interfaces could be observed (Figs. 3(b) and 4 (a)), and these dislocations were pinned well by the IL, as shown by HRTEM images in Figs. 3(c) and 4(b). It indicates that the IL not only plays the role of transferring load between C$_f$ and matrix, but also has the role of pinning dislocations. According to the previous studies [8,9], the IL was composed of nano-grains with soft amorphous grain boundaries (GBs). Due to the high density of dislocations in the Mg matrix and the small size of micro-particles in the IL, the dislocation tips are inevitably close to soft GBs and almost intersected at some points, as shown in Fig. 3(c) and (d).

After pre-stretching to 440 MPa (80% of its tensile strength), the 45 vol.%Al$_2$O$_3$@C$_f$/Mg was observed with HRTEM. As expected, some interfacial micro-cracks were found in the pre-stretched sample (Fig. 5 (a)). The width of micro-crack was so small that both sides of micro-crack could be taken in one HRTEM image, as shown in Fig. 5(b). Obviously, the right side in Fig. 5(b) was C$_f$ and almost no IL phases (MgO) remained on the surface of C$_f$, which was consistent with the previous fracture analysis (Fig. 2(b)). Different from the C$_f$ side, some MgO nano-grains could be observed in the side of Mg matrix, and no damage was formed between IL and Mg matrix, as shown in Fig. 5(c). It is obvious that the interfacial micro-crack propagated along the interface between IL and C$_f$. As a result, the profile of interfacial micro-crack is relatively smooth, similar to the surface of C$_f$.

For comparison, 45 vol.%YSZ@C$_f$/Mg was also pre-stretched to 864 MPa (80% of its tensile strength), and then the interfacial microstructure was observed with HRTEM, as shown in Fig. 6. As anticipated, the interfacial micro-crack had been found as well, and the two sides of interfacial micro-crack were respectively Mg matrix and C$_f$, as shown in Fig. 6(a). Correspondingly, the HRTEM observation was carried out at the same location, as shown in Fig. 6(b) and (c). On the Mg matrix side, some MgO nano-grains was remained and bonded well with Mg matrix (Fig. 6(b)). On the other side, part of IL still remained on the surface of C$_f$, and bonded well with the C$_f$ (Fig. 6(c)). In order to analyze the nanostructure clearly, higher magnification of image was taken at the micro-crack edge of the C$_f$ side, as shown in Fig. 6(d). Combined with Fig. 6(b), it is clarified that both sides of interfacial micro-crack are MgO nano-grains. In Fig. 6(c), the GBs of MgO nano-grains were outlined with a dash line and the profile of dash line was similar to the edges of micro-crack. It indicates that the interfacial micro-crack propagates along the soft GBs of MgO nano-grains within the IL. Moreover, the profile of
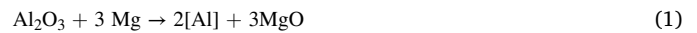
interfacial micro-crack shows jagged-like morphology.

4. Discussion

To optimize the design of the interface, it is necessary to clarify the inherent relationship of following characteristics: (I) the interfacial nanostructures, (II) interfacial stress state, (III) the initiation and propagation of interfacial micro-crack, and (IV) the mechanical properties of C$_f$/Mg.

4.1. The interfacial nanostructures and stress state

At first, it is necessary to review some mechanics of interfacial reaction, because both interfacial nanostructure and stress state are affected significantly by interfacial reaction [8–11]. In the Al$_2$O$_3$@C$_f$/Mg, TiO$_2$@C$_f$/Mg and YSZ@C$_f$/Mg, not only the Mg matrix and coating on the surface of C$_f$ participated in interface reaction, but also C$_f$ could participate in interface reaction in some cases, and the interfacial reactions obeyed following equations, respectively.

$$Al_2O_3 + 3\ Mg \rightarrow 2[Al] + 3MgO \tag{1}$$

$$TiO_2 + 2\ Mg \rightarrow [Ti] + 2MgO \tag{2}$$

$$ZrO_2 + 2\ Mg \rightarrow [Zr] + 2MgO \tag{3}$$

$$[Ti] + C \rightarrow TiC \tag{4}$$

$$[Zr] + C \rightarrow ZrC \tag{5}$$

Unlike Al element having a high solubility in the Mg matrix [8], the reduced Ti [8] and Zr [9] are difficult to dissolve into the Mg matrix and formed a high concentration zone in the Mg matrix nearby the interface. As a result, part of Ti and Zr could react with C$_f$ and formed a small quantity of in-situ carbide (TiC and ZrC) on the surfaces of C$_f$ (Eq. 4 and 5). As well known, a moderate interfacial reaction can improve the interfacial bonding strength [11,16], and the excessive interfacial reactions can inevitably damage the performance of C$_f$ [16]. In the present study, it is considered that the formation of a small number of in-situ carbides is appropriate and beneficial to improve the bonding strength. This can be confirmed by the high strengthening ratios of the TiO$_2$@C$_f$/Mg (about 80%) and YSZ@C$_f$/Mg (about 90%).

On the contrast, no carbide (Al$_4$C$_3$) was formed in Al$_2$O$_3$@C$_f$/Mg [8]. At the same time, Mg and carbon were chemically inert, so C$_f$ bonded directly with the MgO IL. Taking account of the poor compatibility between C$_f$ and most of oxides [1], the interface between C$_f$ and MgO IL is believed to be a weak bonding.

According to previous studies [8,9], the interfacial reactions (Eqs. (1)–(3)) would cause 21.8%, 8.7% and 7.63% volume expansion (as listed in Table 2), respectively. As a result, a great deal of crystalline defects (such as soft amorphous GBs) could be formed [8,39], and the larger the volume expansion was, the severer the interfacial crystal defects were [8,9]. According to the above HRTEM observations (Figs. 4 and 5), after pre-stretching with 440 MPa and 540 MPa, the interfacial micro-cracks were formed in 45 vol% Al$_2$O$_3$@C$_f$/Mg, but no obvious interfacial damage could be found in 45 vol% YSZ@C$_f$/Mg Even if the latter's stress was higher. This indicates that there seems to be a certain relationship between the strengthening ratio and the interface crystal defects.

Additionally, a large thermal residual stress (TRS) with a tensile state would form in the IL due to the mismatch of thermal expansion coefficient between C$_f$ and IL [21,40,41]. Our previous investigation indicates [9] that some ZrO$_2$ nano-grains could remain in the IL of YSZ@C$_f$/Mg, and the phase transformation of ZrO$_2$ from tetragonal to monoclinic could relax the TRS of IL.

Though all the IL were mainly composed of MgO nano-grains and the thickness of IL (about 20 nm) were similar, the size of MgO nano-grains were quite different. In Al$_2$O$_3$@C$_f$/Mg, the size of MgO nano-grains was
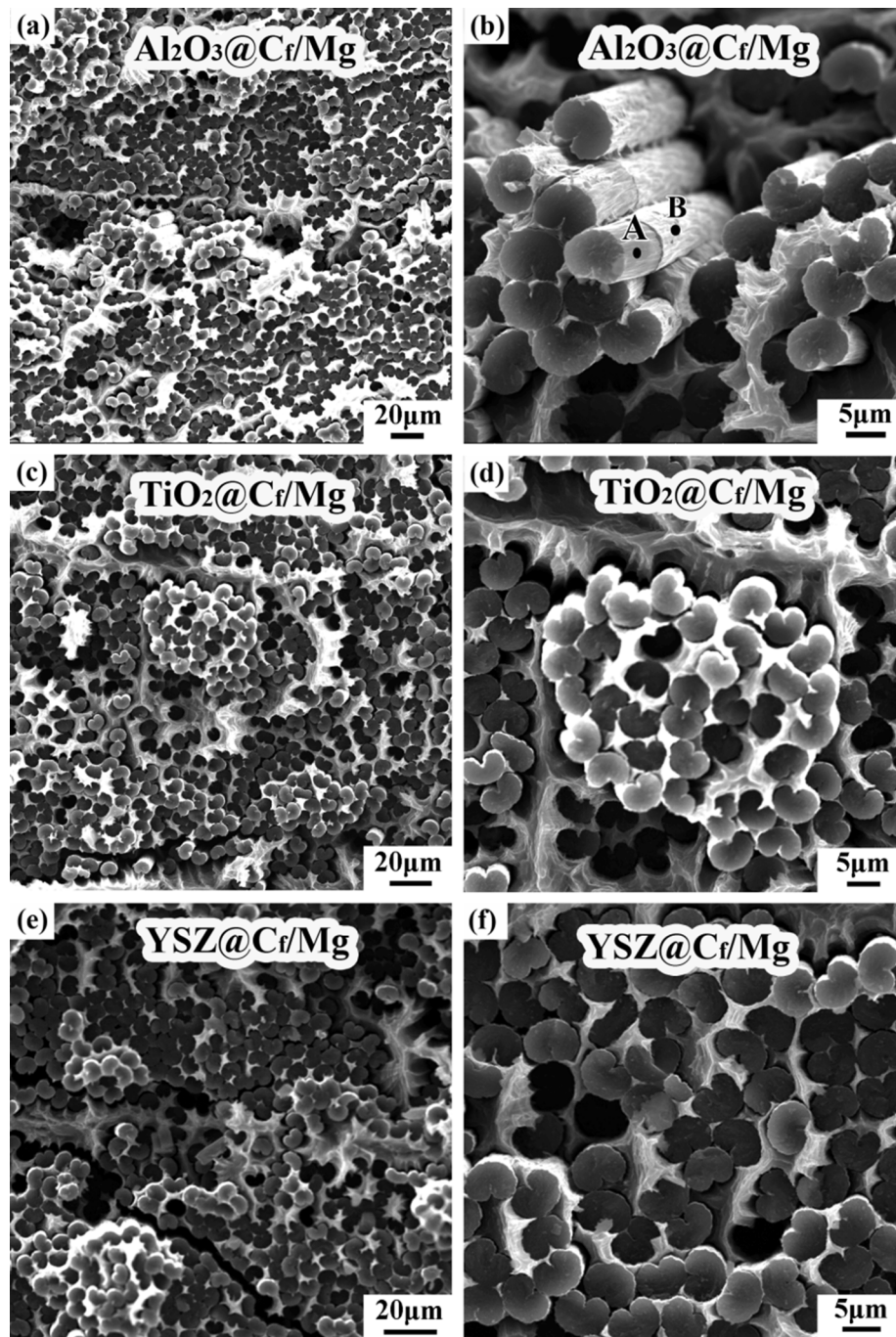
Fig 2. SEM fractographs of 45 vol% C_f/Mg composites: (a) and (b) Al_2O_3 coatings, (c) and (d) TiO_2 coating, (e) and (f) YSZ coating.

about 10 ~ 20 nm and larger than that in TiO_2@C_f/Mg (3–5 nm) and YSZ@C_f/Mg (3–5 nm), as listed in Table 2. As a result, the IL in Al_2O_3@C_f/Mg was almost composed of one to two layers of MgO nano-grains. But in TiO_2@C_f/Mg and YSZ@C_f/Mg, the IL consisted of multi-layer of MgO nano-grains. According to Fig. 6, it was concluded that multi-layered nanostructures could provide "zigzag" pathway for the interfacial micro-crack propagation.

To better and more intuitively compare the fabrication processing and characteristics of C_f/Mg, the experimental results are in detail listed in Table 2.

As well known, the interfacial microstructures[1,10], TRS [41,42] and C_f direction [43,44] are the most important factors affecting the mechanical properties of composites reinforced with continuous fiber. According to Table 1, it is obvious that the strengthening ratio was unrelated to the volume fraction of C_f, although the distribution of TRS would be affected by the volume fraction of C_f. According to the previous study [42], it was clarified that TRS would decrease slowly with increasing fiber spacing in unidirectional fiber-reinforced metal matrix composite. In this study, the difference of fiber spacing in 35 vol.%C_f/Mg and 45 vol.%C_f/Mg are small (0.33 μm), indicating that the TRS did not change much. Since C_f was unidirectionally aligned and the tensile direction of composite was parallel to the longitudinal direction of C_f, the C_f direction effect could also be neglected in this study. Therefore, the strengthening ratio could only be determined by interfacial micro-structure. Conversely, the strengthening ratio could also be considered as an important indicator for the evaluation of the interface microstructure.
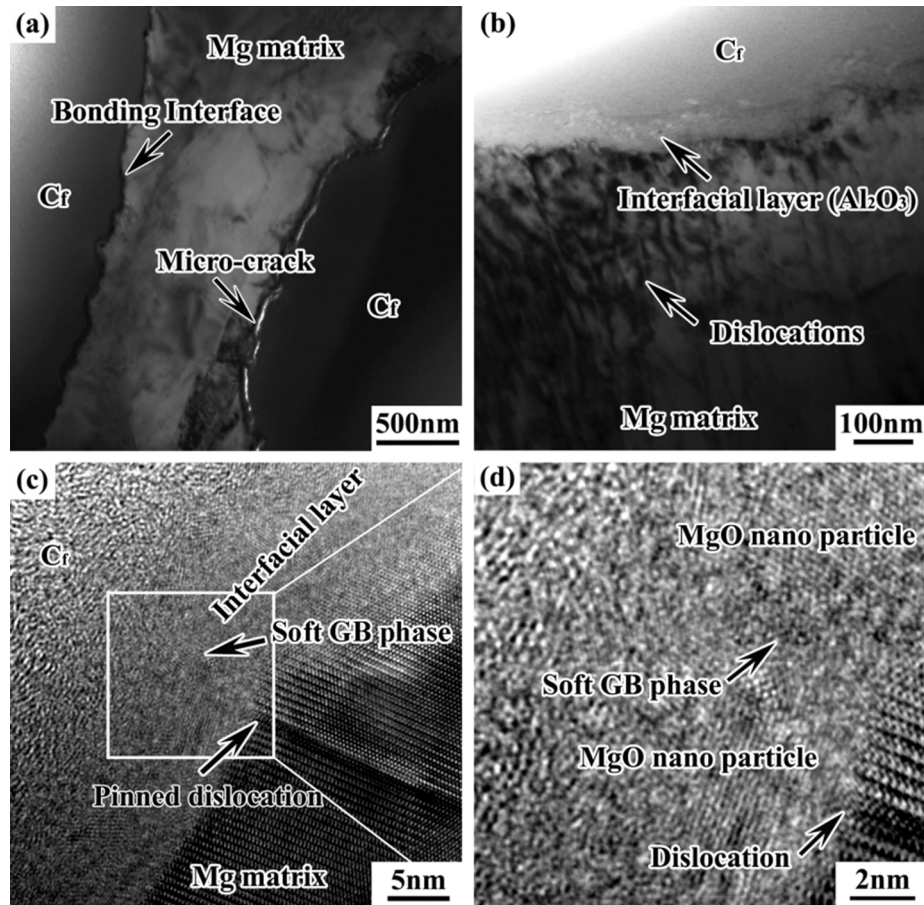
Fig 3. Microstructures nearby the interface in 45 vol% Al₂O₃@C_f/Mg after pre-stretching (440 MPa): (a) bonding interface and interfacial microstructure, (b) dislocation nearby the interface, (c) interfacial nanostructure and (d) nanostructure of IL.
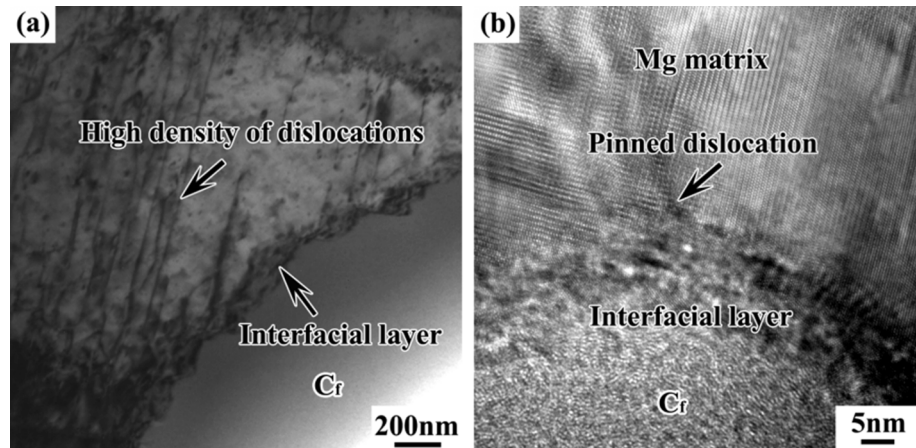

Fig 4. (a) TEM image of interfacial microstructure and (b) HRTEM image interfacial nanostructure in 45vol.%YSZ@C_f/Mg pre-stretched to 540 MPa.

4.2. The initiation and propagation of interfacial micro-crack

According to the previous studies[8,9], a large compressive stress could be induced due to the volume expansion caused by the interfacial reaction. As a result, the nanocrystalline particles and disordered intergranular boundaries (soft amorphous phases) would be formed in the interfacial layer. The soft GBs can also be found in the Fig. 3(d) and 6 (d). In the view of interfacial microstructures of the pre-stretched 45 vol % Al₂O₃@C_f/Mg and 45 vol% YSZ@C_f/Mg (Figs. 3 and 4), high density dislocations pinned by the IL could be found in the Mg matrix. Of course,

these high-density dislocations cannot be completely attributed to the pre-stretch. The TRS can also form a plastic deformation zone in the matrix nearby C_f/matrix interface [45–47]. The dislocation tips and soft GBs were so close that they almost intersect at one point (Figs. 3 and 4), due to the small size of nano-grains of the IL and the high density of dislocations. Except for the stress field induced by dislocation pile-up, TRS and shear stress (caused by load transfer) further deteriorated the stress state of the IL. As the pre-stretch stress (induced by external load) gradually increased, the interface gradually approached the critical state. According to previous studies [8,39], the soft GBs could be
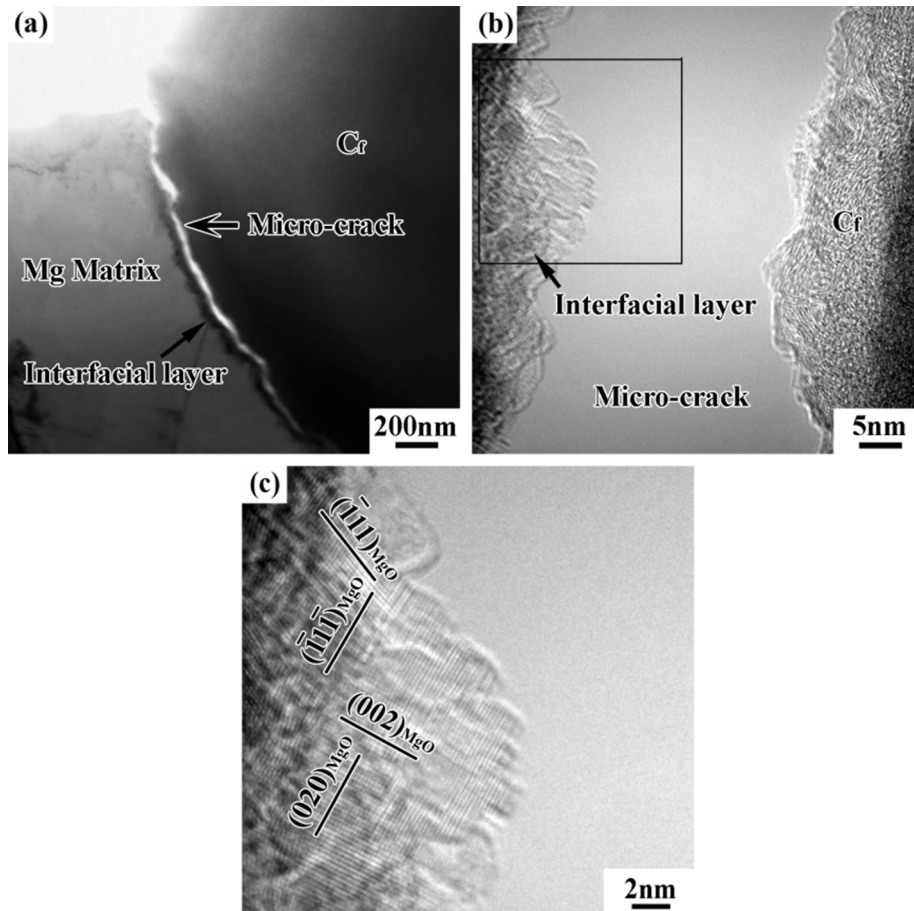
Fig 5. (a) TEM and (b) HRTEM images of interfacial microstructure in $Al_2O_3@C_f/Mg$, and (c) high magnification image of region framed with black lines in Fig. 5(b).

considered as the weakest zone of the IL. Therefore, for the $Al_2O_3@C_f/Mg$, the interfacial micro-crack preferred to initiate at the soft GBs of the IL (with aggravated lattice defects) under the actions of multiple stress fields, even with lower pre-stretch stress (440 MPa). Then, the interfacial micro-cracks rapidly spread to the surface of C_f and propagated along the interface between C_f and IL, resulting in interfacial debonding and rapid failure of $Al_2O_3@C_f/Mg$. As a result, some annular steps could be found on the tensile fractograph of $Al_2O_3@C_f/Mg$ (Fig. 2(b)), and the $Al_2O_3@C_f/Mg$ exhibited the poorest tensile properties and strengthening ratio (Table 1).

Unlike that in the 45 vol.%$Al_2O_3@C_f/Mg$, no interfacial micro-crack could be found in 45 vol.%$YSZ@C_f/Mg$ pre-stretched with a tensile stress of 540 MPa (50% of its tensile strength). By comparing the interfacial characteristics of $Al_2O_3@C_f/Mg$ and $YSZ@C_f/Mg$ listed in Table 2, it was obvious that the delay of interfacial micro-crack initiation was attributed to the slight crystalline defects (soft amorphous GBs) and the lower TRS (relaxed by phase transformation of the remaining ZrO_2). After pre-stretching with a tensile stress of 864 MPa (80% of its tensile strength), the interfacial micro-crack could be found in $YSZ@C_f/Mg$ (Fig. 6). Like that in the $Al_2O_3@C_f/Mg$, the interfacial micro-crack initiated at the soft GBs of the IL in $YSZ@C_f/Mg$, under the action of multiple stress fields. Nevertheless, the interfacial micro-cracks did not propagate along the interface between C_f and IL, but along the soft GBs within the IL. This ought be attributed to the multi-layer nanostructure of IL (composed of multi-layer of nano-grains), which provided multiple paths for the propagation of interfacial micro-cracks, resulting in a jagged-like profile (Fig. 6). Obviously, the jagged-like micro-cracks could absorb more energy than the smooth profile of micro-cracks in $Al_2O_3@C_f/Mg$. Moreover, it is considered that the formation of trace ZrC also plays a positive role in improving the bonding strength between C_f and IL.

4.3. The interface failure mechanism and tensile properties of C_f/Mg

In order to better describe the interfacial nanostructures, stress state and failure behaviors of the C_f/Mg composites, the schematic diagrams are drawn from the longitudinal section (Fig. 7(a)) and transverse section (Fig. 7(b), (c), (d) and (e)).

In Fig. 7(a), the multiple stress fields in the C_f/Mg composite is depicted, including the stress induced by dislocation pile-up, the shear stress formed by load transfer and the longitudinal tensile TRS caused by the large mismatch of CTE between the C_f and IL. According to previous studies [40], the maximum of the TRS in the IL was hoop stress and tensile, as shown in Fig. 7(b) and (d). Of course, the TRS of IL in $YSZ@C_f/Mg$ is lower than that in $Al_2O_3@C_f/Mg$ due to the phase transformation of ZrO_2. At the same time, the crystal defects (soft amorphous GBs) of the IL in $Al_2O_3@C_f/Mg$ is heavier (Fig. 7(b)).

Since the soft GBs could be considered as the weakest zone of the IL, taking account of the multiple stress fields and microstructural crystal defects, obviously the GBs of the IL was the critical position for micro-crack initiation. As the external load increased to 440 MPa, the interfacial micro-cracks inevitably initiated at the ILs in $Al_2O_3@C_f/Mg$, then there were almost no other paths, and interfacial micro-cracks could only propagate through the interface between IL and C_f, as shown in Fig. 7(c). On the other hand, only when the axial load further increased to 864 MPa, the interfacial micro-cracks initiated in $YSZ@C_f/Mg$, as shown in Fig. 7(d). Differently, the multi-layer nanostructure provided multiple paths for the propagation of interfacial micro-cracks. Due to the soft amorphous GBs, the interfacial micro-cracks propagate along the GBs within the IL, as shown in Fig. 7(e). Therefore, the propagation path
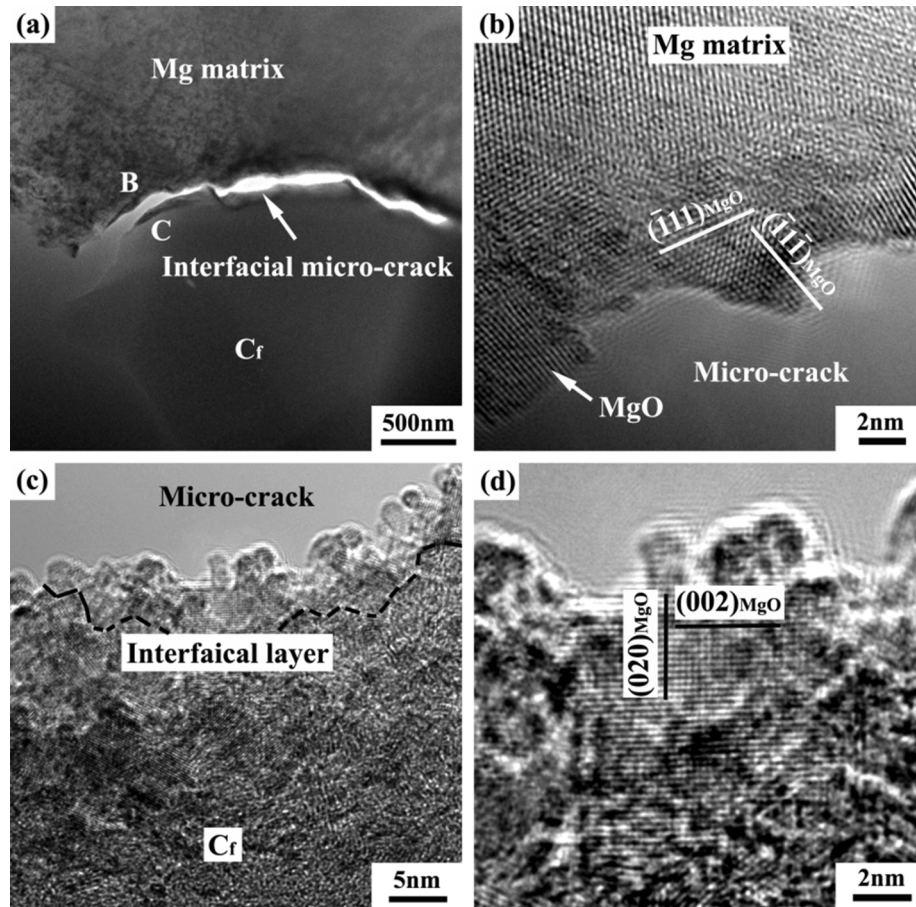
Fig 6. (a) HRTEM image of IL in YSZ@C_f/Mg; (b) and (c) magnified image of regions B and C marked in Fig. 7(a), respectively; (d) magnified image of Fig. 7(c).

Table 2

The contrast list of fabrication processing and interfacial characteristics of Al$_2$O$_3$@C_f/Mg, TiO$_2$@C_f/Mg and YSZ@C_f/Mg.

Fabrication processing and interfacial characteristics	Al$_2$O$_3$	TiO$_2$	YSZ
Preparation of C_f preforms	Filament winding technique		
Fabrication of CfMMCs	Vacuum pressureless infiltration processing		
Thickness of IL	About 20 nm [8]	About 20 nm [8]	About 20 nm [9]
The size of nano-grains of IL	10 ~ 20 nm [8]	3 ~ 5 nm [8]	3 ~ 5 nm [9]
Chemical composition of IL	MgO [8]	MgO and a small quantity of TiC [8]	MgO, a small quantity of ZrC and ZrO$_2$ [9]
Volume expansion rate caused by interfacial reaction	21.8% [8]	8.7% [8]	7.63% [9]
Phase transformation in the IL	No [8]	No [8]	Yes [9]
Relaxation of TRS	No [8]	No [8]	Yes [9]
Lattice defects in the IL	Heavy [8]	Moderate [8]	Slight [9]
Propagation route of micro-crack	Along the surface of C_f	—	Along the GBs within the IL
Micro-crack profile	Smooth	—	Jagged-like
Interface bonding of IL/C_f	Relative weak	—	Relative strong
Tensile strength of CfMMCs	The lowest	Higher	The highest
The strengthening ratio	The lowest	Higher	The highest

of micro-cracks is similar to the profiles of GBs, showing jagged-like. As a supplement, the moderate formation of carbides on the surface of C_f is beneficial to avoid the propagation of micro-crack between the IL and the C_f. Nevertheless, excessive carbide formation may cause etching of C_f surfaces, and this kind of etching may be fatal to relatively brittle C_f. How to quantitatively evaluate the effects of surface etching on the mechanical properties of C_f will be the next research direction.

The above schematic diagram and analysis are consistent with the mechanical properties of C_f/Mg. Though the tensile strength of C_f/Mg showed a significant difference, it revealed a clear regularity. As discussed previously, the tensile strength of C_f/Mg was proportional to the volume fraction of C_f, but the strengthening ratios were independent of the volume fraction of C_f, as shown in Table 1. Since the tensile strength of as-cast Mg was very low (less than 100 MPa) compared with C_f, the strengthening ratios could also be thought as strengthening efficiency of C_f. Therefore, this parameter could also provide a new mean to evaluate the interfacial optimization of C_f reinforced composites.

For the sake of optimizing the IL nanostructure design and promoting the properties of C_f/Mg, following factors should be taken into account as much as possible: (I) multi-layer of nanostructure, (II) moderate interfacial reaction (forming a small quantity of in-situ carbides), (III) TRS relaxation (such as by phase transformation of ZrO$_2$ etc.) and (IV) the slighter crystalline defects.

5. Conclusions

In this study, the Al$_2$O$_3$@C_f/Mg, TiO$_2$@C_f/Mg and YSZ@C_f/Mg were prepared with vacuum pressureless infiltration processing. Through microstructural observation, the inherent relationships among the interfacial reaction, microstructures and stress state, the initiation and
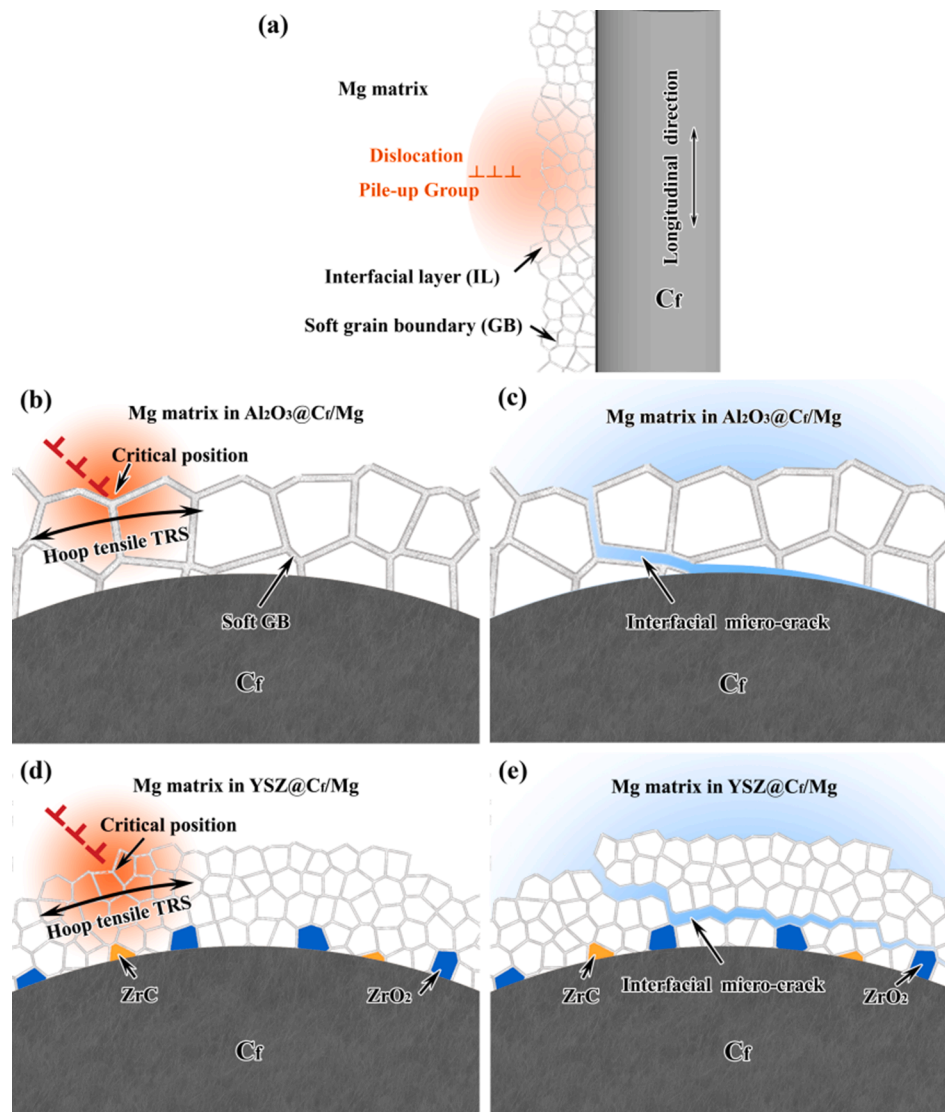
Fig 7. Sketch map of interfacial micro-crack evaluation: (a) longitudinal section, (b) and (c) transverse section of Al$_2$O$_3$@C$_f$/Mg before and after the initiation of interfacial micro-crack, (d) and (e) transverse section of YSZ@C$_f$/Mg before and after the initiation of interfacial micro-crack.

propagation of interfacial micro-crack and mechanical properties of C$_f$/Mg were clarified. The following conclusions could be obtained:

(1) The strengthening ratios of C$_f$/Mg were independent of the volume fraction of C$_f$ and determined mainly by the interfacial microstructures, and the strengthening ratio of Al$_2$O$_3$@C$_f$/Mg, TiO$_2$@C$_f$/Mg and YSZ@C$_f$/Mg were 45%, 80% and 90%, respectively.

(2) Under the actions of multiple stress fields, the interfacial micro-cracks would prefer to initiate at the soft GBs of the IL, but the propagation of interfacial micro-cracks were different. In Al$_2$O$_3$@C$_f$/Mg, the interfacial micro-crack propagated along the interface between C$_f$ and IL due to the poor compatibility; while in YSZ@C$_f$/Mg, the interfacial micro-crack propagated along the soft GBs within the IL due to the multi-layer nanostructure of IL.

(3) The excellent tensile properties of YSZ@C$_f$/Mg could be attributed to the jagged-like interfacial micro-cracks due to the absorption of more energy.

Declaration of Competing Interest

The authors declare that they have no known competing financial interests or personal relationships that could have appeared to influence the work reported in this paper.

References

[1] Shirvanimoghaddam K, Hamim SU, Karbalaei Akbari M, Fakhrhoseini SM, Khayyam H, Pakseresht AH, et al. Carbon fiber reinforced metal matrix composites: Fabrication processes and properties. Compos A Appl Sci Manuf 2017;92:70–96.

[2] Chung DDL. In: 9 - Metal-Matrix Composites. Carbon Composites (Second Edition): Butterworth-Heinemann; 2017. p. 532–62.

[3] Rawal SP. Metal-matrix composites for space applications. JOM. 2001;53(4):14–7.

[4] Chawla KK. Metal Matrix Composites. Composite Materials: Science and Engineering. In: Chawla KK, editor. Composite Materials: Science and Engineering. Cham: Springer International Publishing; 2019. p. 199–249. https://doi.org/10.1007/978-3-030-28983-6_6.

[5] Arkhurst BM, Seol JB, Lee YS, Lee M, Kim JH. Interfacial structure and bonding mechanism of AZ31/carbon-fiber-reinforced plastic composites fabricated by thermal laser joining. Compos B Eng 2019;167:71–82.

[6] Song M, Wu G, Yang W, Jia W, Xiu Z, Chen G. Mechanical Properties of Cf/Mg Composites Fabricated by Pressure Infiltration Method. J Mater Sci Technol 2010; 26(10):931–5.

[7] Hufenbach W, Andrich M, Langkamp A, Czulak A. Fabrication technology and material characterization of carbon fibre reinforced magnesium. J Mater Process Technol 2006;175(1-3):218–24.

[8] Wang WG, Xiao BL, Ma ZY. Interfacial reaction and nanostructures in Mg matrix composites reinforced with carbon fibers modified by sol–gel method. Compos Sci Technol 2013;87:69–76.

[9] Wang WG, Xiao BL, Ma ZY. Evolution of interfacial nanostructures and stress states in Mg matrix composites reinforced with coated continuous carbon fibers. Compos Sci Technol 2012;72(2):152–8.

[10] Li S, Qi L, Zhang T, Zhou J, Li H. Interfacial microstructure and tensile properties of carbon fiber reinforced Mg–Al-RE matrix composites. J Alloy Compd 2016;663: 686–92.

[11] Zhang S, Chen G, Pei R, Hussain M, Wang Y, Li D, et al. Effect of Gd content on interfacial microstructures and mechanical properties of Cf/Mg composite. Mater Des 2015;65:567–74.

[12] Korb G, Koráb J, Groboth G. Thermal expansion behaviour of unidirectional carbon-fibre-reinforced copper-matrix composites. Compos A 1998;29(12):1563–7.

[13] Mykura H, Mykura N. Thermal expansion and stress relaxation of metal-matrix composites. Compos Sci Technol 1992;45(4):307–12.

[14] Pradere C, Sauder C. Transverse and longitudinal coefficient of thermal expansion of carbon fibers at high temperatures. Carbon 2008;46(14):1874–84.

[15] Viala JC, Claveyrolas G, Bosselet F, Bouix J. The chemical behaviour of carbon fibres in magnesium base Mg-Al alloys. J Mater Sci 2000;35(7):1813–25.

[16] N. Chawla KKC. Interface. Metal Matrix Composites. Boston, MA: Springer US; 2006. p. 113-36.

[17] Wang X, Chen GQ, Li B, Wu GH, Jiang DM. Microstructure and mechanical properties of graphite fiber-reinforced high-purity aluminum matrix composite. J Mater Sci 2009;44(16):4303–7.

[18] Abidin AZ, Kozera R, Höhn M, Endler I, Knaut M, Boczkowska A, et al. Preparation and characterization of CVD-TiN-coated carbon fibers for applications in metal matrix composites. Thin Solid Films 2015;589:479–86.

[19] Liang J, Saha MC, Altan MC. Effect of Carbon Nanofibers on Thermal Conductivity of Carbon Fiber Reinforced Composites. Procedia Eng 2013;56:814–20.

[20] Baklanova NI, Zaitsev BN, Titov AT, Zima TM. The chemistry, morphology, topography of titanium carbide modified carbon fibers. Carbon 2008;46(2): 261–71.

[21] Gupta N, Nguyen NQ, Rohatgi PK. Analysis of active cooling through nickel coated carbon fibers in the solidification processing of aluminum matrix composites. Compos B Eng 2011;42(4):916–25.

[22] Pei ZL, Li K, Gong J, Shi NL, Elangovan E, Sun C. Micro-structural and tensile strength analyses on the magnesium matrix composites reinforced with coated carbon fiber. J Mater Sci 2009;44(15):4124–31.

[23] Constantin L, Fan L, Zou Q, Thomas B, Roger J, Heintz J-M, et al. Design of tailored oxide-carbide coating on carbon fibers for a robust copper/carbon interphase. Carbon 2020;158:607–14.

[24] Baumli P, Sychev J, Budai I, Szabo JT, Kaptay G. Fabrication of carbon fiber reinforced aluminum matrix composites via a titanium-ion containing flux. Compos A Appl Sci Manuf 2013;44:47–50.

[25] Ureña A, Rams J, Escalera MD, Sánchez M. Effect of copper electroless coatings on the interaction between a molten Al–Si–Mg alloy and coated short carbon fibres. Compos A Appl Sci Manuf 2007;38(8):1947–56.

[26] Abdel Gawad O, Abou Tabl MH, Abdel Hamid Z, Mostafa SF. Electroplating of chromium and Cr-carbide coating for carbon fiber. Surf Coat Technol 2006;201(3-4):1357–62.

[27] Xue Y, Chen W, Zhao Q, Fu YongQing. Electroless carbon fibers: A new route for improving mechanical property and wettability of composites. Surf Coat Technol 2019;358:409–15.

[28] Suzuki T, Umehara H. Pitch-based carbon fiber microstructure and texture and compatibility with aluminum coated using chemical vapor deposition. Carbon 1999;37(1):47–59.

[29] Qi L, Li S, Zhang T, Zhou J, Li H. An analysis of the factors affecting strengthening in carbon fiber reinforced magnesium composites. Compos Struct 2019;209: 328–36.

[30] Wu F, Zhu J, Ibe K, Oikawa T. Analysis of the interface in graphite/magnesium composites at the nanometer scale. Compos Sci Technol 1998;58(1):77–82.

[31] Zhenhai X. Role of coatings in axial tensile strength of long fibre-reinforced metal-matrix composites. Acta Metall Mater 1993;41(7):2097–104.

[32] Chowdhury ASMF, Mari D, Schaller R. The effect of the orientation of the basal plane on the mechanical loss in magnesium matrix composites studied by mechanical spectroscopy. Acta Mater 2010;58(7):2555–63.

[33] Chand S. Review Carbon fibers for composites. J Mater Sci 2000;35(6):1303–13.

[34] Zhu Z, Kuang X, Carotenuto G, Nicolais L. Fabrication and properties of carbon fibre-reinforced copper composite by controlled three-step electrodeposition. J Mater Sci 1997;32(4):1061–7.

[35] Dorfman S, Mundim KC, Fuks D, Berner A, Ellis DE, Van Humbeeck J. Atomistic study of interaction zone at copper–carbon interfaces. Mater Sci Eng, C 2001;15(1-2):191–3.

[36] Hao X, Nie H, Ye Z, Luo Yi, Zheng L, Liang W. Mechanical properties of a novel fiber metal laminate based on a carbon fiber reinforced Zn-Al alloy composite. Mater Sci Eng, A 2019;740-741:218–25.

[37] Riggs DM, Shuford RJ, Lewis RW. Graphite Fibers and Composites. In: Lubin G, editor. Handbook of Composites. Boston, MA: Springer, US; 1982. p. 196–271.

[38] Paris O, Peterlik H. The structure of carbon fibres. In: Eichhorn SJ, Hearle JWS, Jaffe M, Kikutani T, editors. Handbook of Textile Fibre Structure, 10. Woodhead Publishing; 2009. p. 353–77.

[39] Szlufarska I, Nakano A, Vashishta P. A Crossover in the Mechanical Response of Nanocrystalline Ceramics. Science 2005;309(5736):911–4.

[40] Huang B, Yang Y, Luo H, Yuan M, Chen Y. Effect of the interfacial reaction layer thickness on the thermal residual stresses in SiCf/Ti-6Al-4V composites. Mater Sci Eng, A 2008;489(1-2):178–86.

[41] Akser EO, Choy K-L. Finite element analysis of the stress distribution in a thermally and transversely loaded Ti-6Al-4V/SiC fibre composite. Compos A Appl Sci Manuf 2001;32(2):243–51.

[42] Sheng Li D, Wisnom MR. Finite element micromechanical modelling of unidirectional fibre-reinforced metal-matrix composites. Compos Sci Technol 1994;51(4):545–63.

[43] Zeng Q, Sun L, Ge J, Wu W, Liang J, Fang D. Damage characterization and numerical simulation of shear experiment of plain woven glass-fiber reinforced composites based on 3D geometric reconstruction. Compos Struct 2020;233: 111746. https://doi.org/10.1016/j.compstruct.2019.111746.

[44] Blanc R, Germain Ch, costa JPD, Baylou P, Cataldi M. Fiber orientation measurements in composite materials. Compos A Appl Sci Manuf 2006;37(2): 197–206.

[45] Meguid SA, Shagal G, Paskaramoorthy R. On the local elastic-plastic behaviour of the interface in titanium/silicon carbide composites. Compos A Appl Sci Manuf 2002;33(12):1629–40.

[46] Trojanová Z, Lukáč P, Riehemann W, Mordike BL. Study of relaxation of residual internal stress in Mg composites by internal friction. Mater Sci Eng, A 2002;324(1-2):122–6.

[47] Cao X, Shi Q, Liu D, Feng Z, Liu Qu, Chen G. Fabrication of in situ carbon fiber/ aluminum composites via friction stir processing: Evaluation of microstructural, mechanical and tribological behaviors. Compos B Eng 2018;139:97–105.